Journal of Colloid and Interface Science 348 (2010) 289–292

Contents lists available at ScienceDirect

Journal of Colloid and Interface Science

www.elsevier.com/locate/jcis

Short Communication

Oriented growth behavior of Ag nanoparticles using SDS as a shape director

Zhenquan Tan *, Hiroya Abe, Makio Naito, Satoshi Ohara

Joining and Welding Research Institute, Osaka University, 11-1 Mihogaoka, Ibaraki, Osaka 567-0047, Japan

ARTICLE INFO

Article history:
Received 3 February 2010
Accepted 8 April 2010
Available online 18 May 2010

Keywords:
Ag nanoparticles
SDS
Shape control
Soft template

ABSTRACT

We report a chemical approach for synthesizing shape-controlled Ag nanoparticles by using the surfactant SDS as a soft template. The experimental approach includes a two-step reaction: the first step is quickly generating Ag seed clusters by a chemical reaction using sodium borohydride as a reducing reagent; the second is the slow growth of controllable Ag nanoparticles by a mild chemical reaction using hydroxylamine hydrochloride as a reducing reagent. Spherical, polyhedral, and fibrous Ag nanoparticles are synthesized successfully in aqueous solution having SDS concentrations of 0.01, 0.02, and 0.2 wt.%, respectively. Size, morphology, and dispersion stability of these Ag nanoparticles depend on the concentrations of both SDS and $AgNO_3$.

1. Introduction

Silver (Ag) nanoparticles are very useful in many fields, such as nanocatalysts [1], biological labeling [2], optoelectronics [3], and surface-enhanced Raman scattering (SERS) [4]. Since the physical, chemical, and electronic behaviors of metal nanoparticles are determined partially by the size and the crystalline morphology [5–8], shape-controllable synthesis of defined Ag nanoparticles has attracted significant research interest. A variety of approaches have been developed to synthesize Ag nanoparticles with well-defined structures [9–15]. Recently, surfactants such as sodium bis(2-ethylhexyl) sulfosuccinate (AOT) [12,16,17] and sodium dodecyl sulfate (SDS) [18–21] have been used to synthesize Ag nanoparticles. Such surfactants have been used for nanoparticle synthesis because when the concentration of a selected surfactant is higher than the critical micelle concentration (CMC), the surfactant can form micromicelles which act as a soft template to control the size and the shape of target nanoparticles. Although the small and narrow size distribution of the obtained Ag nanoparticles is easily controlled by the soft template characteristics of the surfactants [16,18,22], the formation of the shape-controlled Ag nanoparticles assisted by a surfactant template has not been as successful [10,11,16]. Consequently this aspect remains a significant challenge for chemists and material scientists. The concentration and the surrounding medium of the surfactant have been reported to influence the shape and the size of the synthesized nanoparticles [23,24]. However, there have been only a handful of studies focusing on the growth orientation behavior at concentrations below the CMC.

Here, we report the chemical synthesis of Ag nanoparticles, in which the shape of the nanoparticles is controlled by SDS at concentrations below the CMC in water. The experiment involves a two-step reaction. The first step involves the rapid synthesis of Ag seed clusters by a simple chemical reaction using sodium borohydride ($NaBH_4$) as a reducing reagent. The second step involves the slow crystal growth of Ag nanoparticles by a mild chemical reduction with hydroxylamine hydrochloride ($NH_2OH{\cdot}HCl$). This reagent has been reported as a mild reducing reagent which allows Ag nanoparticles to grow on the preproduced seed clusters while avoiding the formation of new isolated Ag clusters [25]. Lofton and Sigmund have reported that the nucleation and growth kinetics play an important role in the formation of shape-controlled nanoparticles, as well as the thermodynamics and physical constrictions [26]. The rapid first-stage reaction can homogeneously produce numerous Ag seed clusters. The slow crystal growth stage provides a suitable environment to easily control the growth of specific crystal faces and form Ag nanoparticles with well-defined shapes. Here, the growth behavior of Ag nanoparticles is investigated in an SDS aqueous solution which is below the SDS CMC value.

2. Experimental

The designed synthesis approach for Ag nanoparticles is presented in Scheme 1. Initially, a 1-ml aqueous solution of silver nitride ($AgNO_3$; 0.2 M) was added to 40 ml distilled water containing a certain amount of SDS. Various amounts of SDS were used in this experiment: 0.01, 0.02, 0.05, 0.125, 0.2, and 0.3 wt.%. The solutions were mixed completely by ultrasonic treatment. A 1-ml aqueous solution of $NaBH_4$ (0.1 M) was slowly added into the mixed solution of $AgNO_3$ and SDS while vigorously stirring. The

* Corresponding author. Fax: +81 6 6879 4370.
E-mail address: zq-tan@jwri.osaka-u.ac.jp (Z. Tan).

0021-9797/$ - see front matter © 2010 Elsevier Inc. All rights reserved.
doi:10.1016/j.jcis.2010.04.018

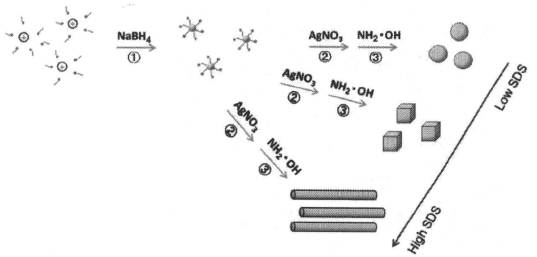

Scheme 1. Experimental approach for the synthesis of Ag nanostructures using SDS as a soft template.

mixed solution changed from colorless to a dark-yellow color, indicating the formation of Ag clusters. In the crystal growth reaction, another 0.5 ml of $AgNO_3$ aqueous solution was added to 10 ml of the Ag cluster suspension and mixed completely by stirring for 10 min. Subsequently, an aqueous hydroxylamine hydrochloride solution (0.05 mM) was slowly added into the mixed dispersion to reduce the Ag^+ ions. During the second step, constant mild stirring was employed. The morphology of the as-grown Ag nanoparticles obtained in the second stage was characterized by a field-emission scanning electron microscope (FE-SEM; Hitachi SU-70, Japan).

3. Results and discussion

Fig. 1 shows the sizes of the resulting Ag seed clusters prepared in the first stage as determined by dynamic light scattering (DLS) measurements using a particle size analyzer (Microtrac UPA-UT151, Nikkiso, Japan) (also see the Supporting material, Fig. S1). The Ag seed clusters were several hundred nanometers in size when the concentration of SDS was very low (0.01 wt.%). Ag seed clusters aggregated under this condition because the low concentration of SDS could not effectively disperse the Ag clusters. As the SDS concentration was increased, the Ag seed clusters dramatically reduced in size. At 0.02 wt.% SDS solution, the Ag clusters had an average size of 47.5 nm. The size of Ag clusters was almost below 10 nm when the SDS concentration was higher than 0.05 wt.%. Transmission electron microscope (TEM) images of Ag clusters are exhibited in Fig. S2. At 0.05 wt.% SDS, the resulting Ag clusters were spherical shape. The ellipsoidal and rod-like clusters increased with the concentration of SDS, which may due to the influence of SDS concentration. The additional intermediate plane can also be observed in such SDS-stabilized Ag clusters by the TEM investigation. Ag clusters have a narrow size distribution (Figs. S1C–F), which is in agreement with previous studies [16,18,22]. The results clearly showed that the sizes of the Ag seed clusters were dependent on the SDS concentration. Since the concentration of 0.05 wt.% is much lower than the CMC of SDS in water (0.0081 M) [27], our results suggest that SDS acts as a dispersing agent to effectively prevent Ag clusters aggregating in the aqueous solution. In addition, when Ag seed clusters grew, the sizes of the as-grown Ag nanoparticles were also closely related to the SDS concentration (Fig. 2). Deposits of Ag nanoparticles at low SDS concentrations are observed (0.01 and 0.02 wt.%) because the detergent concentration is not high enough to prevent aggregation of Ag nanoparticles in aqueous solution. The Ag nanoparticles following the second-step procedure were well-dispersed in the aqueous solutions when the concentration of SDS was higher than 0.05 wt.%. The sizes of the Ag nanoparticles grown in high SDS concentrations were generally smaller than the sizes of the nanoparticles grown in low SDS concentrations. This was due to the protection of the Ag nanoparticles by SDS.

Fig. 3A shows the FE-SEM images of the as-grown Ag nanoparticles produced in 0.01 wt.% SDS aqueous solution. The resulting Ag

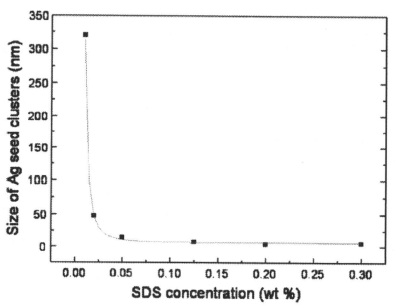

Fig. 1. Changes in the size distribution of the Ag seed clusters with increasing SDS concentrations determined by DLS measurement.

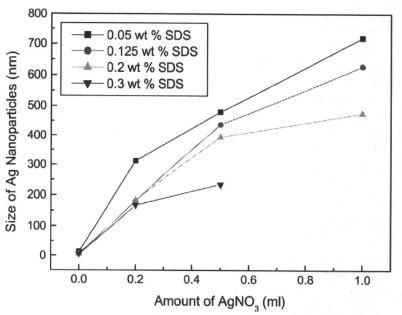

Fig. 2. Changes in the DLS size distribution of the Ag nanocrystals after the second-step crystal growth.

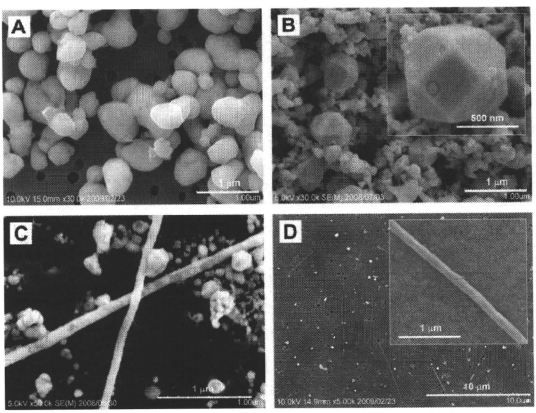

Fig. 3. SEM images of the as-grown Ag nanoparticles: (A) 0.01 wt.% SDS, (B) 0.02 wt.% SDS, (C) 0.125 wt.% SDS, and (D) 0.2 wt.% SDS, following completion of the second-step reaction.

nanoparticles are clearly irregular in appearance and formed approximately spherical shapes. This observation suggests that the crystal growth from the Ag seed cluster to Ag nanoparticles was homogeneous and isotropic at very low concentrations of SDS and this led to the formation of spherical Ag nanoparticles following the second stage. In the case of the 0.02 wt.% SDS solution, the as-grown Ag nanoparticles were anisotropic polyhedral nanostructures (Fig. 3B). Faces and edges were clearly observed and represented a polyhedral nanoparticle with 12-faces. This nanostructure is similar to the truncated octahedral (TO) nanoparticles illustrated by Wang [28]. An XRD pattern of this sample is exhibited in Fig. S3. The diffraction peaks from Ag (1 1 1), (2 0 0), (2 2 0), and (3 1 1) were clearly observed. However, several unexpected peaks were also observed at 22.5°, 29°, and 35°. These peaks originated from the impurities prepared in the second stage. Since hydroxylamine hydrochloride has been reported as a mild reducing reagent [29,30], the results have shown that the slow reaction process aids the quasi-stable crystal growth along the anisotropic directions, even when the concentration of SDS is well below the CMC in water. The formation of polyhedral Ag nanoparticles was also observed in the 0.05 wt.% SDS aqueous solution. Fig. 3C shows the fibrous Ag nanoparticles synthesized in the 0.125 wt.% SDS aqueous solution. Ag nanofibers were formed when the Ag seed clusters grew along specific directions which were determined by the SDS effect. At an SDS concentration of 0.2 wt.%, which is close to the CMC of SDS in water, Ag nanofibers were also formed due to the nanoparticles growing in specific directions. The obtained Ag nanofibers are particularly more attractive than the nanofibers presented in Fig. 3C. Interestingly, XRD patterns of such Ag nanofibers showed that the crystal facet of Ag (3 1 1) was dramatically reduced (Fig. S3). This observation may be due to the anisotropic crystal growth directed by SDS was well as Cl^- ions [12]. Some groups have reported the synthesis of Ag nanofibers using SDS as a soft template in which the SDS concentration is much higher than the CMC [18,21]. The results presented herein give the first example that Ag nanofibers can be synthesized in an SDS aqueous solution lower than the CMC using a two-step chemical reduction approach.

We have characterized the resulting Ag nanoparticles by EDX measurement. Ag nanoparticles were dropped onto a polymeric membrane and dried in air. Ag nanoparticles on the membrane film were sputtered by Au before the EDX measurement. The obtained EDX pattern is shown in Fig. 4. The inset SEM image shows an isolated polyhedral Ag nanoparticle for EDX measurement. The centric spot on the Ag nanoparticle indicates the measured spot of EDX measurement. Numerous signal peaks were clearly observed. Most of them were assigned to Ag, Au, and C elements. Au and C signals come from the Au that sputtered on the membrane film and the polymeric membrane, respectively.

Many research groups have studied the shape-directing influence of SDS for the formation of anisotropic Ag nanoparticles [18–21]. As described by Yang et al. [20], SDS may play two important roles in the crystal growth process. One was that SDS acts as a stabilizer of Ag nanoparticles in the aqueous solution, and the other was that SDS creates a conducive environment and induces the chemically repining for the anisotropic growth of Ag nanoparticles. On the other hand, Pileni discussed that selective adsorption of ions played a more important role during the anisotropic crystal growth than the nature of the templates [12], supported by many experimental data [31–33]. Actually, Yang also demonstrated the role of ions in the formation of anisotropic Ag nanoparticles [20]. In our study, Cl^- ions may be numerously produced by the reaction of hydroxylamine hydrochloride in the second stage. Therefore, it is speculated that both the SDS concentration and the existence of Cl^- ions may play important roles for the formation of polyhedral and fibrous Ag nanoparticles. Initially, numerous Ag seed clusters are homogeneously synthesized by a fast $NaBH_4$ reduction in an aqueous SDS solution. Such Ag seed clusters are approximately spherical in morphology and have a narrow size distribution. SDS molecules are absorbed onto the surface of the Ag seed clusters and prevent Ag nanoparticle agglomeration. The growth rates of the Ag seed clusters at the second step along various directions and the shape of the resulting nanoparticles were determined by the particular reaction environment [26], that is, the concentration of the absorbed SDS and the existence of Cl^- ions. As a result,

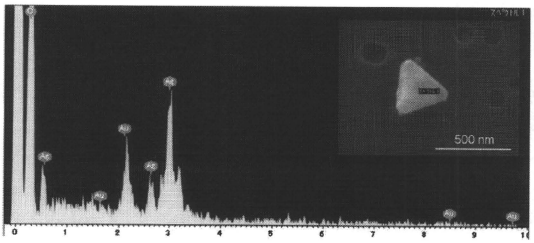

Fig. 4. EDX pattern of an individual Ag nanoparticles obtained in 0.02 wt.% SDS aqueous solution.

polyhedral and fibrous Ag nanoparticles were obtained via a anisotropic crystal growth process (Fig. 3).

4. Conclusion

In summary, a two-step chemical reaction approach for synthesizing the anisotropic Ag nanoparticles was developed by using SDS as a stabilizing agent and a shape director in aqueous solution. The two-step approach includes the rapid preparation of homogeneous Ag seed clusters followed by a slow crystal growth process. The anisotropic crystal growth along specific directions was achieved by controlling the concentration of SDS, and the existence of Cl^- ions. Spherical, polyhedral, and fibrous Ag nanoparticles were successfully synthesized by the described two-step method under conditions that the concentrations of SDS were lower than CMC. It is considered that this two-step process has merit that the nucleation and the crystal growth can be separated; therefore, the anisotropic crystal growth can be easily controlled by change of the chemical environment. This simple method may provide a possible approach to the synthesis of other anisotropic metal nanoparticles, such as Au, Pt, and Pd, for various potential applications.

Acknowledgment

This work was partially supported by a Scientific Research Grant from the Ministry of Education, Culture, Sports, Science, and Technology of Japan.

References

[1] J.-Z. Guo, H. Cui, W. Zhou, W. Wang, J. Photochem. Photobiol., A: Chem. 193 (2008) 89.
[2] H. Cai, Y. Xu, N. Zhu, P. He, Y. Fang, Analyst 127 (2002) 803.
[3] R. Temirov, S. Soubatch, A. Luican, F.S. Tautz, Nature 444 (2006) 350.
[4] G. Braun, S.J. Lee, M. Dante, T.-Q. Nguyen, M. Moskovits, N. Reich, J. Am. Chem. Soc. 129 (2007) 6378.
[5] R.M. Rioux, H. Song, M. Grass, S. Habas, K. Niesz, J.D. Hoefelmeyer, P. Yang, G.A. Somorjai, Top. Catal. 39 (2006) 167.
[6] C.J. Murphy, N.R. Jana, Adv. Mater. 14 (2002) 80.
[7] F. Kim, J.H. Song, P. Yang, J. Am. Chem. Soc. 124 (2002) 14316.
[8] L.M. Falicov, G.A. Somorjai, Proc. Natl. Acad. Sci. USA 82 (1985) 2207.
[9] Y. Sun, Y. Xia, Science 298 (2002) 2176.
[10] R.R. Naik, S.J. Stringer, G. Agarwal, S.E. Jones, M.O. Stone, Nat. Mater. 1 (2002) 169.
[11] M.H. Huang, A. Choudrey, P. Yang, Chem. Commun. (2000) 1063.
[12] M.-P. Pileni, Nat. Mater. 2 (2003) 145.
[13] B. Wiley, Y. Sun, B. Mayers, Y. Xia, Chem. Eur. J. 11 (2005) 454.
[14] A.R. Tao, S. Habas, P. Yang, Small 4 (2008) 310.
[15] C.J. Murphy, T.K. Sau, A.M. Gole, C.J. Orendorff, J. Gao, L. Gou, S.E. Hunyadi, T. Li, J. Phys. Chem. B 109 (2005) 13857.
[16] C. Petit, P. Lixon, M.-P. Pileni, J. Phys. Chem. 97 (1993) 12974.
[17] S. Mandal, S.K. Arumugam, R. Pasricha, M. Sastry, Bull. Mater. Sci. 28 (2005) 503.
[18] Y.-H. Chen, C.-S. Yeh, Colloids Surf., A 197 (2002) 133.
[19] C.-C. Yang, C.-C. Wan, Y.-Y. Wang, J. Colloid Interface Sci. 279 (2004) 433.
[20] J. Yang, Q. Zhang, J.Y. Lee, H.-P. Too, J. Colloid Interface Sci. 308 (2007) 157.
[21] X.C. Song, Y. Zhao, Y.F. Zheng, E. Yang, J. Fu, Y. He, Cryst. Growth Des. 8 (2008) 1823.
[22] F. Mafuné, J. Kohno, Y. Takeda, T. Kondow, H. Sawabe, J. Phys. Chem. B 104 (2000) 9111.
[23] P.A. Brugger, P. Cuendet, J. Am. Chem. Soc. 103 (1981) 2923.
[24] E. Braun, Y. Eichen, U. Sivan, Nature 391 (1998) 775.
[25] K.R. Brown, M.J. Natan, Langmuir 14 (1998) 726.
[26] C. Lofton, W. Sigmund, Adv. Funct. Mater. 15 (2005) 1197.
[27] J. Israelachvili, Intermolecular and Surface Forces, Academic Press, San Diego, 1997. p. 355.
[28] Z.L. Wang, J. Phys. Chem. B 104 (2000) 1153.
[29] T. Onodera, Z. Tan, A. Masuhara, H. Oikawa, H. Kasai, H. Nakanishi, T. Sekiguchi, Jpn. J. Appl. Phys. 45 (2006) 379.
[30] Z. Tan, H. Xu, H. Abe, M. Naito, S. Ohara, J. Nanosci. Nanotechnol. 10 (2010) 3978.
[31] T.S. Ahmadi, Z.L. Wang, A. Heinglein, M.A. El Sayed, Chem. Mater. 8 (1996) 1161.
[32] K. Esumi, K. Matsuhira, K. Torigoe, Langmuir 11 (1995) 3285.
[33] A. Henglein, M. Giersig, J. Phys. Chem. 104 (2000) 6767.

NANO LETTERS

LETTER

pubs.acs.org/NanoLett

Extra-Low-Temperature Oxygen Storage Capacity of CeO_2 Nanocrystals with Cubic Facets

Jing Zhang,[⊥,†] Hitoshi Kumagai,[‡] Kae Yamamura,[‡] Satoshi Ohara,[#,†] Seiichi Takami,[†] Akira Morikawa,[‡] Hirofumi Shinjoh,[‡] Kenji Kaneko,[§] Tadafumi Adschiri,[*,†,∥] and Akihiko Suda[*,‡]

[†]Institute of Multidisciplinary Research for Advanced Materials (IMRAM), Tohoku University, 2-1-1, Katahira, Aoba-ku, Sendai 980-8577, Japan

[‡]Catalyst Lab., Sustainable Mater. Div., Toyota Central Research & Development Laboratories, Inc., 41-1, Nagakute, Aichi 480-1192, Japan

[§]Department of Material Science and Engineering, Kyushu University, 744, Motooka, Nishi-ku, Fukuoka 819-0395, Japan

[∥]Advanced Institute for Materials Research (AIMR), Tohoku University, Japan

Supporting Information

ABSTRACT: Herein we demonstrate the extra-low-temperature oxygen storage capacity (OSC) of cerium oxide nanocrystals with cubic (100) facets. A considerable OSC occurs at 150 °C without active species loading. This temperature is 250 °C lower than that of irregularly shaped cerium oxide. This result indicates that cubic (100) facets of cerium oxide have the characteristics to be a superior low-temperature catalyst.

KEYWORDS: Cerium oxide, nanocrystals, cubic facets, oxygen storage capacity, catalyst

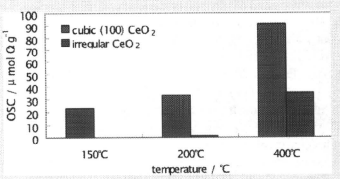

Cerium oxide has received much attention due to its ability as a three-way catalyst in the exhaust system of automobiles[1,2] and as primary oxygen storage material.[2,3] Because the catalytic activity of cerium oxide originates from the surface oxygen,[4] the active oxygen content at the cerium oxide surface must be increased to improve catalytic activities. Cerium oxide is a highly stable fluorite structure and a one-electron redox agent. The effective ionic radii of Ce^{4+} and O^{2-} are 0.10 and 0.14 nm, respectively;[5] the relative ionic radius of Ce^{4+}/O^{2-} is 0.71, resulting in a coordination number of cerium to oxygen atoms of 8 and that of oxygen to cerium atoms of 4. This 8 to 4 coordination permits oxide defects in $CeO_{(2-X)}$ over a wide range of X values, which approach 0.5.[6] Previous experimental and theoretical studies have shown that increasing the specific surface area can optimize the catalytic activity of cerium oxide.[7]

Recently, an alternative strategy to enhance the oxygen storage capacity (OSC) of cerium oxide has been introduced by modifying the morphology of cerium oxide.[8−10] In particular, the (100) facet of cerium oxide is the best catalytic candidate for highly reactive surfaces.[8] The six (100) planes have the highest surface energy among the low-index crystal planes. This high surface energy originates from the instability of the top-layer oxygen, which is located at the bridging positions between two cerium ions.[11]

Herein, we propose a modified approach to fabricate cerium oxide nanocrystals with a controlled size of about 10 nm that is morphologically bound by six (100) planes via an organic-ligand-assisted supercritical hydrothermal process.[12,13] Interestingly, cerium oxide nanocrystals with six (100) facets show an enhanced OSC performance at lower temperature compared to those with irregular morphologies. The extra-low-temperature OSC of the cerium oxide nanocrystals with cubic (100) facets described herein opens a route for low-temperature industrial applications such as innovative exhaust catalysts.

Cerium oxide nanocrystals with cubic (100) facets were prepared by a modified hydrothermal synthesis.[12,13] The cerium oxide precursor was precipitated from 0.1 M of a cerium(III) nitrate aqueous solution by adding 25% ammonia aqueous solution in a 100 mL glass beaker while stirring with a magnetic stirrer. The freshly prepared cerium oxide precursor with water (2.5 mL, 0.02 M−Ce) and hexanoic acid (0.2 mL) was transferred into a pressure-resistant SUS316 vessel (inner volume, 5 mL). The supercritical hydrothermal synthesis was carried out in the reaction vessel at 400 °C for 10 min. The reaction vessel was then allowed to cool in a water bath. The aggregated nanocrystals were filtered, subsequently washed with water and ethanol, and then dried in air. A comparable sample of irregularly shaped cerium oxide powder was also prepared by calcination of the cerium oxide precursor at 400 °C for 10 min.

The samples were analyzed using a Nicolet AVATAR 360 FT-IR spectrometer to measure the infrared (IR) spectra, a Hitachi

Received: August 4, 2010
Revised: December 11, 2010
Published: January 4, 2011

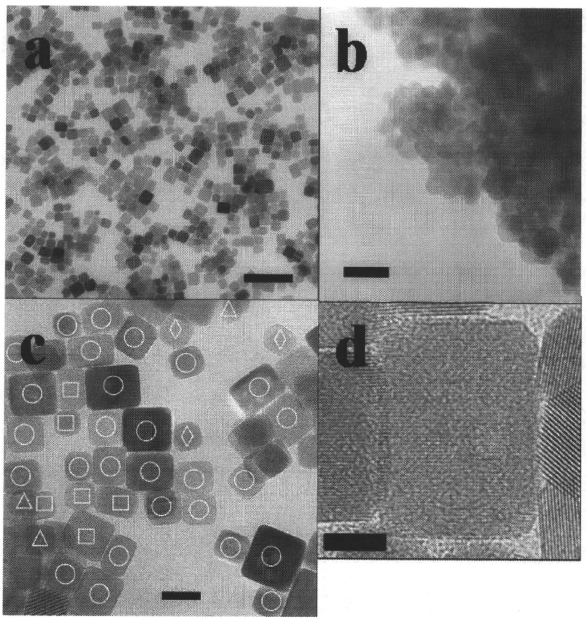

Figure 1. (a) TEM image of cerium oxide nanocrystals with cubic (100) facets. Scale bar, 50 nm. (b) TEM image of an irregular shape cerium oxide powder. Scale bar, 20 nm. (c) TEM image of cerium oxide nanocrystals with cubic (100) facets with group markings. Circles correspond to the first group with a {200} waffle pattern. Squares correspond to the second group with {200}{220} lattice fringe. Diamonds correspond to the third group with {110} lattice fringe. Triangles correspond to the fourth group with {111} lattice fringe. Scale bar, 10 nm. (d) High-resolution TEM image of cubic cerium oxide nanocrystals. Scale bar, 5 nm.

H-9000UHR for conventional TEM observations, and FEI TECNAI-20 for three-dimensional TEM observations. Thermogravimetric (TG) analysis was carried out by a Shimadzu TGA-50 from room temperature to 400 °C under a 20% O_2 (N_2-balanced) atmosphere, and then the OSC was calculated from the weight loss and gain after several cycles of reduction and oxidation. Cerium oxide nanocrystals with (100) facets were initially treated at 150 °C for 1 h in air to remove hexanoic acid from the surface. The sample was oxidized in 20% O_2 (N_2-balanced) and then reduced in 12% H_2 (N_2-balanced) and oxidized repeatedly at 150, 200, and 400 °C. (See Figure S1, Supporting Information.) The BET surface area was measured on a Micro Data automatic surface area analyzer model 4232.

Regardless of the synthetic method (supercritical hydrothermal process or calcinations), the X-ray diffraction patterns of both samples correspond to the cubic fluorite structure of CeO_2 (Figure S2, Supporting Information). Figure S3 (Supporting Information) shows the IR spectra of the hydrothermally synthesized sample before and after TG measurements. The IR spectrum prior to the TG measurements has strong absorption bands in the 2800−3000 cm^{-1} regions, which are attributed to the C−H stretching mode of the methyl and methylene groups. The other bands at 1530 and 1540 cm^{-1} originate from the stretching frequencies of the carboxylate group. The presence of these bands indicates bonding between the organic ligand molecules and the surface of the nanocrystals, which leads to the formation of cerium oxide nanocrystals with cubic (100) facets. This structural feature is very similar to the cerium oxide nanocrystals prepared with decanoic acid.[12] An abrupt weight loss is observed around 150 °C in the TG trace of the as-prepared hydrothermally synthesized sample (Figure S4, Supporting Information). Additionally, the characteristic absorption bands are absent in the IR spectrum from the sample after the TG measurements. Thus, the weight loss of the sample is simply due to the loss of an organic moiety from the crystal surface.

Panels a and b of Figure 1 show the conventional TEM images of cerium oxide nanocrystals prepared by supercritical hydrothermal synthesis with hexanoic acid and by calcination of the cerium oxide precursor, respectively. As shown in Figure 1a, the cerium oxide crystals prepared by supercritical hydrothermal synthesis exhibit a highly dispersed square shape with an average size of about 10 nm, whereas the cerium oxide powder prepared

dx.doi.org/10.1021/nl102738n |*Nano Lett.* 2011, 11, 361–364

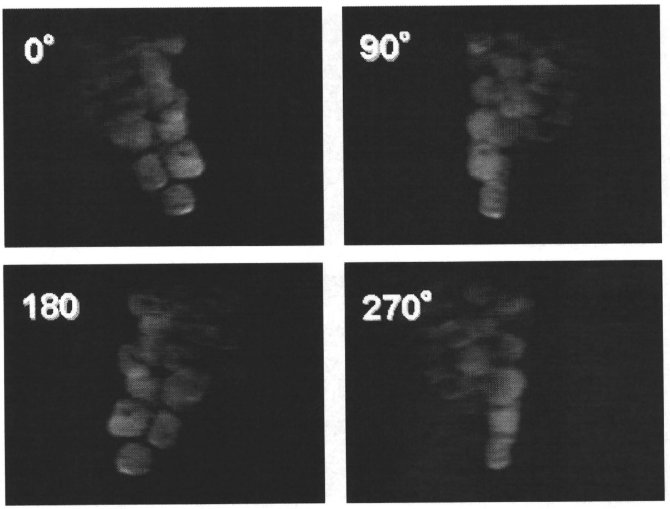

Figure 2. 3D TEM images corresponding to the clockwise rotation of the structure at 0°, 90°, 180°, and 270° of an aggregated powder of cerium oxide nanocrystals with cubic (100) facets.

by calcination consists of aggregated crystallites with irregular morphologies. The particle sizes of irregular cerium oxide nanoparticles were about 10 nm, which is consistent with the average crystallite size calculated from the XRD peaks using the Scherrer equation. Figure 1c is a high-magnification micrograph of hydrothermally synthesized particles. Figure S5 (Supporting Information) shows the electron beam diffraction pattern corresponding to the area of Figure 1c. The electron beam diffraction pattern reveals that all the detectable reflections are indexed to the same positions as those of the cubic fluorite structure of CeO_2, and the {200} diffraction has a relatively high intensity.

The individual cerium oxide nanocrystals can be classified into four groups by reverse-Fourier transformation of the lattice image of each cerium oxide nanocrystal lined up on the carbon film grid of TEM (Figure S6, Supporting Information). Nearly 70% of the crystals (marked by circles) are classified as the first group with {200}, which corresponds to cerium oxide nanocrystals with cubic (100) facets. Figure 1d shows a magnified image in which the waffle pattern can be observed. Fifteen percent of the crystals can be classified as the second group (denoted by squares in Figure 1c), which shows a {200} {220} lattice fringe. Although the second group also displays {200} lattice fringes, orthogonal stripes could not be observed, which may be because the second group is inclined to the carbon film grid of the TEM. It is highly likely that the second group is cerium oxide nanocrystals with cubic (100) facets. The remaining crystals are evenly divided between the third (denoted by diamonds) and fourth (denoted by triangles) groups, which show {110} lattice fringes and {111} lattice fringes, respectively. Therefore, it is considered that the ceria nanocrystals prepared by

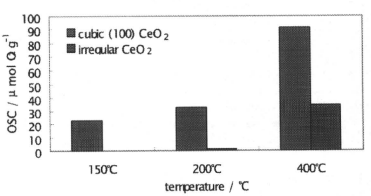

Figure 3. Comparative OSC of cerium oxide nanocrystals with cubic (100) facets and a sample of irregularly shaped cerium oxide powder.

supercritical hydrothermal synthesis may have two kinds of shape; main nanocrystals are cube and/or slightly truncated cube[13] and the remaining other smaller ones are truncated octahedron. Furthermore, we successfully produced a three-dimensional reconstructed image of the cerium oxide nanocrystals with {200}. Figure 2 shows four still photographs; each 3D image corresponds to the clockwise rotation of the structure at 0°, 90°, 180°, and 270°. These images support the assertion that cerium oxide nanocrystals have cubic morphologies with (100) facets and not a thin plate shape.

Figure 3 compares the OSC of the two different types of cerium oxide nanocrystals, the one with cubic (100) facets and the other with an irregular morphology, at different temperatures. The BET surface areas of cubic and irregular cerium oxide nanocrystals are 61 and 100 m^2/g, respectively. Two differences are identified. Although the cubic nanocrystals have a smaller

dx.doi.org/10.1021/nl102738n |*Nano Lett.* 2011, 11, 361–364

surface area than the irregular particles, the OSC of cerium oxide nanocrystals with cubic (100) facets is nearly 2.6 times higher at 400 °C. Additionally, the effective activating temperature of OSC is 150 °C for the cerium oxide nanocrystals with cubic (100) facets, but 400 °C for the irregular morphologies with a low OSC.

The BET surface area of cerium oxide nanocrystals with cubic (100) facets is 61 m^2/g, whereas the calculated surface area for 1 g of 10 nm cubic CeO_2 crystallites is 137.0 m^2/g. The calculated and the measured values seem to be consistent, considering the aggregation level of each crystallite observed in Figures 1a, 1c, and 2. Highly dispersed and ordered particles could easily result in a strong aggregation, which reduces the effective BET surface area. Assuming that two of the four oxygen sites are involved in the OSC process, the estimated[11] number of the surface oxygen atoms is 5.7 μmol of O_2/m^2. Hence, the theoretical OSC is calculated to be 357 μmol of O_2/g for 61 m^2/g.

There are two reasons that the theoretical OSC is much higher than the measured value in Figure 3. First, the activation energy is insufficient for the remaining oxygen to be released, particularly at 150 and 200 °C. Second, the cerium oxide nanocrystals can degrade at 400 °C; the cerium oxide nanocrystals with cubic (100) facets do not maintain their cubic morphology after 5 h of reduction and oxidation treatments at 400 °C (Figure S7, Supporting Information). Hence, lanthanum ions were introduced into the nanocrystals to improve the thermal stability of the cerium oxide nanocrystals with cubic (100) facets. Figure S8 (Supporting Information) shows TEM images of lanthanum-containing cerium oxide nanocrystals; these crystals form similar nanocrystals with cubic morphologies. Further characterization of La-containing cerium oxide nanocrystals is in progress.

In summary, single-crystalline cerium oxide nanocrystals with dimensions of about 10 nm with (100) facets were synthesized via organic ligand-assisted supercritical hydrothermal syntheses. The extra-low-temperature OSC performance was confirmed in cerium oxide nanocrystals with cubic (100) facets by comparing the OSC performance of the cubic nanocrystals to that of the irregularly shaped cerium oxide. We expect that this work will aid in the development of a shape-controlled synthetic methodology for inorganic nanocrystals. Furthermore, these cubic nanocrystals show promise in the design of catalytic materials with higher performances by controlling the formation of well-defined crystal planes.

■ ASSOCIATED CONTENT

Supporting Information. Figures of TG analysis for OSC, X-ray diffraction patterns, IR spectra, an electron beam diffraction pattern, and TEM images. This material is available free of charge via the Internet at http://pubs.acs.org.

■ AUTHOR INFORMATION

Corresponding Author

*E-mail address: ajiri@tagen.tohoku.ac.jp (T.A.); a-suda@mosk.tytlabs.co.jp (A.S.).

Present Addresses

[⊥]Chinese Academy of Science, China.

[#]Joining and Welding Research Institute, Osaka University, Japan.

■ ACKNOWLEDGMENT

We thank T. Nakayama and K. Niihara of Nagaoka University of Technology for showing us the future prospects of this research on the crystal face control of ceria.

■ REFERENCES

(1) Kummer, J. T. *Proc. Energy Combust. Sci.* **1980,** *6,* 177.

(2) Yao, H. C.; Yao, Y. F. Yu *J. Catal.* **1984,** *86,* 254–265.

(3) Di Monte, R.; Kasper, J.; Bradshaw, H.; Norman, C. *J. Rare Earth* **2008,** *26,* 136–140.

(4) Tanabe, T.; et al. *Stud. Surf. Sci. Catal.* **2001,** *138,* 135–144.

(5) Shannon, R. D.; Prewitt, C. T. *Acta Crystallogr., Sect. B* **1969,** *25,* 925–946.

(6) Wu, L. J.; et al. *Phys. Rev. B* **2004,** *69,* No. 125415.

(7) Masui, T.; Fujiwara, K.; Machida, K.; Adachi, G. *Chem. Mater.* **1997,** *9,* 2197–2204.

(8) Skorodumova, N. V.; Baudin, M.; Hermansson, K. *Phys. Rev. B* **2004,** *69,* No. 075401.

(9) Mai, H. X.; Sun, L.-D.; Zhang, Y.-W.; Si, R.; Feng, W.; Zhang, H.-P.; Liu, H.-C.; Yan, C.-H. *J. Phys. Chem. B* **2005,** *109,* 24380–24385.

(10) Zhou, K.; et al. *J. Catal.* **2005,** *229,* 206–212.

(11) Norenberg, H.; Harding, J. H. *Surf. Sci.* **2001,** *477,* 17–24.

(12) Zhang, J.; et al. *Adv. Mater.* **2007,** *19,* 203–206.

(13) Kaneko, K.; Inoke, K.; Freitag, B.; Hungria, A. B.; Midgley, P. A.; Hansen, T. W.; Zhang, J.; Ohara, S.; Adschiri, T. *Nano Lett.* **2007,** *7,* 421–425.

J|A|C|S COMMUNICATIONS

Published on Web 02/03/2010

Selective Growth of Monoclinic and Tetragonal Zirconia Nanocrystals

Kazuyoshi Sato,* Hiroya Abe, and Satoshi Ohara

Joining and Welding Research Institute, Osaka University, 11-1 Mihogaoka, Ibaraki, Osaka 567-0047 Japan

Received December 19, 2009; E-mail: k-sato@jwri.osaka-u.ac.jp

In this communication, we demonstrate for the first time a selective growth of single-crystalline pure monoclinic and tetragonal ZrO_2 nanocrystals of <10 nm diameter, driven by controlling their surface energy. The growth of metal oxide nanocrystals with a well-organized crystalline phase is of fundamental and technological interest because in this way it is possible to tune their size-dependent unique properties,[1,2] and thus establish their potential application in chemistry, electronics, optics, magnetics, and mechanics. ZrO_2 is a case in point, with a phase-dependent potential application in a number of technologies. Monoclinic ZrO_2 is important for catalysis,[3] gate dielectrics,[4] and bioactive coatings on bone implants,[5] while tetragonal and cubic ZrO_2 are promising candidates for fuel cell electrolytes,[6] oxygen sensors,[7] and phase-transformation-toughened structural materials.[8]

In particular, the growth of pure monoclinic ZrO_2 nanocrystals of <10 nm diameter is a challenging task in the selective growth of the different phases, since a high-temperature tetragonal phase is stable at room temperature as the consequence of the dominance of the surface energy contribution to the Gibbs free energy of formation in this size range.[9] A report by Zhang et al. suggests that the surface energy of oxides can be controlled by capping the surface with an organic substance.[10] They successfully grow the unstable (001) faceted CeO_2 by capping with decanoic acid. Although surface capping-assisted growth using similar anionic substances was also applied to ZrO_2, the resulting nanocrystals of <10 nm diameter still chiefly exhibited a tetragonal phase.[11,12] Herein, we report the facile selective growth route of pure monoclinic and tetragonal ZrO_2 nanocrystals of <10 nm diameter, with and without a cationic capping agent, $N(CH_3)_4^+$.

In a typical procedure, a Zr^{4+} precursor ($ZrOCl_2 \cdot 8H_2O$, 0.01 mol) was dissolved in a basic aqueous solution (pH $\approx$ 10.5) containing a mixture of either $N(CH_3)_4HCO_3$ (tetramethyl-ammonium hydrogen carbonate; TMAHC)/$N(CH_3)_4OH$ (tetramethyl-ammonium hydroxide; TMAH) or $KHCO_3$/KOH. The clear solution of dissolved precursor was transferred into a 50 mL, Teflon-lined, stainless steel autoclave and heat treated at 150 °C. The products were obtained as well-dispersed colloidal solutions. ZrO_2 nanocrystals in the solution were purified by washing ten times with deionized water using ultrafiltration, with a molecular weight cutoff of 3000 for subsequent characterizations. The yield of ZrO_2 nanocrystals was almost 100% in both TMAHC/TMAH and $KHCO_3$/KOH systems. The ZrO_2 nanocrystals were characterized by transmission electron microscopy (TEM; JEOL JEM-2100F) with an accelerating voltage of 200 kV, X-ray diffraction (XRD; JEOL JDX-3530M) with Cu Kα radiation (λ = 0.154178 nm) at 40 kV and 40 mA, Raman spectroscopy (Horiba Jobin Yvon LabRAM ARAMIS) at room temperature with 532 nm excitation line of an diode-pumped solid state laser, and UV−vis adsorption spectroscopy (Shimadzu, UV-2450) with a double-beam recording spectrometer using 1 cm quartz cells.

Figure 1 shows TEM images of ZrO_2 nanocrystals grown in the TMAHC/TMAH and $KHCO_3$/KOH systems. These images clearly

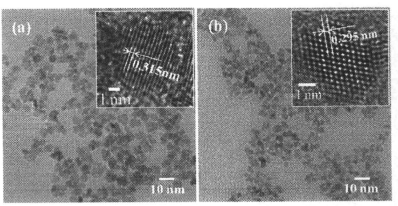

Figure 1. TEM images of ZrO_2 nanocrystals grown in the (a) TMAHC/TMAH and the (b) $KHCO_3$/KOH systems. Each respective inset shows an HRTEM image of an isolated nanocrystal.

indicate that both nanocrystals consist entirely of crystals of a uniform size of <10 nm diameter. The inset shows the high-resolution TEM (HRTEM) image of an isolated nanocrystal, indicating the single-crystalline nature of the nanocrystals grown in both systems. The lattice spacing is 0.315 and 0.295 nm, corresponding to (−111) of monoclinic and (111) of tetragonal ZrO_2 for the nanocrystals grown in the TMAHC/TMAH and the $KHCO_3$/KOH systems, respectively. Figure S-1 (Supporting Information) shows the size distribution of the ZrO_2 nanocrystals in the aqueous solution measured by dynamic light-scattering method, showing the nanocrystals almost perfectly dispersed in the aqueous solution by taking into account that the hydrodynamic diameter overestimates by several nanometers the real size.[13]

The XRD patterns of the powdered nanocrystals shown in Figure 2 further confirm that the respective phases observed in the HRTEM images represent the entire nanocrystals in both systems. The peaks are relatively broad, supporting the very small crystalline size. The sizes estimated by Scherrer's formula using full width of half maxima of (−111) for monoclinic and (111) for tetragonal phases were almost the same at 5.4 and 5.2 nm, respectively. The inset of Figure 2 shows the Raman spectra recorded for colloidal solutions of ZrO_2 nanocrystals. For the nanocrystals grown in the TMAHC/TMAH system, the purely monoclinic structure is confirmed by the observation of 13 Raman modes of the 18 ($9A_{1g} + 9B_{1g}$) expected by symmetry analysis,[14] which provides evidence that the growth of monoclinic ZrO_2 nanocrystals shown above was driven by the surface capping with $N(CH_3)_4^+$ (denoted as TMA^+ in the following text), and not by the surface energy reduction through agglomeration by drying. The broad Raman band for the tetragonal ZrO_2 nanocrystals indicates that they involve highly disordered lattice defects.[14]

Optical absorption spectra of the colloidal ZrO_2 solutions shown in Figure 3 provide information relating to the lattice defects. Two absorption shoulders are clearly observed at around 5.2 and 5.7 eV for the ZrO_2 nanocrystals grown in the TMAHC/TMAH system. These are almost identical to the optical band gaps of bulk monoclinic ZrO_2,[15] indicating less defective lattices.[16] The tetrago-

10.1021/ja910712r

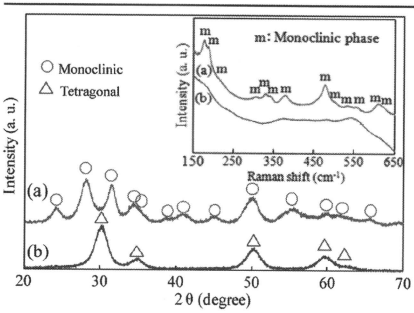

Figure 2. XRD profiles of ZrO_2 nanocrystals grown in the (a) TMAHC/TMAH and the (b) $KHCO_3$/KOH systems. The inset shows Raman spectra of colloidal solutions of ZrO_2 nanocrystals grown in the (a) TMAHC/TMAH and the (b) $KHCO_3$/KOH systems.

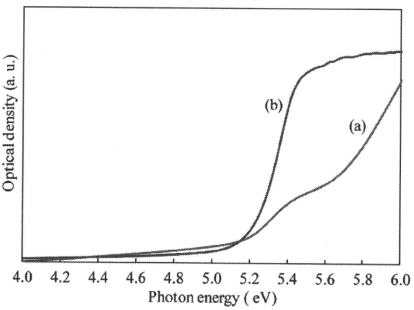

Figure 3. Optical absorption spectra of colloidal solutions of ZrO_2 nanocrystals grown in the (a) TMAHC/TMAH and the (b) $KHCO_3$/KOH systems.

nal ZrO_2 showed only one absorption shoulder at a lower photon energy (approximately at 5.1 eV) than those of monoclinic ZrO_2, indicating the presence of many lattice defects, probably cation impurity and/or oxygen vacancy.[14] Inductively coupled plasma-atomic emission spectroscopy revealed that the concentration of K^+ in the tetragonal ZrO_2 was negligible ($<10^{-7}$ mol·g^{-1}). Thus, it can be concluded that the major lattice defects in the tetragonal ZrO_2 are oxygen vacancies, which is consistent with a previous report.[16]

Here we discuss how the selective growth of monoclinic and tetragonal ZrO_2 nanocrystals was achieved. Monoclinic ZrO_2 nanocrystals may be formed due to the reduction of surface energy through capping with TMA^+, since the capping with organic substances has the potential to reduce the surface energy of oxides by more than 1.7 J·m^{-2} compared with bare surface as suggested by the literature,[10,17,18] while the surface energy of monoclinic ZrO_2 is only approximately 0.4 J·m^{-2} higher than that of tetragonal.[9] The differential thermal analysis (DTA, Figure S-2 in Supporting Information) showed that TMA^+ persists on the nanocrystals up to 280 °C. The considerably higher temperature than the vaporization temperature of free TMAH (157 °C) indicates that TMA^+ successfully caps the surface of ZrO_2 nanocrystals. By contrast, the absence of K^+ in the ZrO_2 grown in the $KHCO_3$/KOH system as shown above indicates that the K^+ does not cap the nanocrystals; thereby, the tetragonal phase is spontaneously formed.[9]

It is suggested that the energy state of surface oxygen plays a vital role in the size-dependent phase stability of ZrO_2 nanocrystals, since the stable phase strongly depends on the sign of charge of the capping agent, i.e., monoclinic ZrO_2 is obtained when the negatively charged surface oxygen is capped with oppositely charged TMA^+. By contrast, the tetragonal phase is stabilized when the nanocrystals are capped with anionic substances,[11,12] in which the surface oxygen may be exposed to the surrounding medium the same as in the case of uncapped nanocrystals ($KHCO_3$/KOH system in this study). The oxygen vacancies in the tetragonal ZrO_2 may be formed as a consequence of relaxation of the unstable surface oxygen.

In summary, our study offers a simple approach for the selective growth of pure monoclinic and tetragonal ZrO_2 nanocrystals of <10 nm diameter capped with and without TMA^+, respectively. The present concept, surface energy control via the capping with an adequate agent, is a promising universal approach to control the crystal phase of technologically important oxide nanocrystals such as Al_2O_3, TiO_2, $BaTiO_3$, and $PbTiO_3$, consequently enabling us to tune their unique properties.

Acknowledgment. This work was supported by a Scientific Research Grant from the Ministry of Education, Science, Sports and Culture of Japan.

Supporting Information Available: Size distributions of colloidal ZrO_2 nanocrystals determined by DLS method (Figure S-1); DTA analysis data of TMA^+-capped ZrO_2 nanocrystals and TMAH pentahydrate (Figure S-2). This material is available free of charge via the Internet at http://pubs.acs.org.

References

(1) Garcia-Barriocanal, J.; Rivera-Calzada, A.; Varela, M.; Sefrioui, Z.; Iborra, E.; Leon, E.; Pennycook, J.; Santamaria, J. *Science* **2008**, *321*, 676.
(2) Hoshina, T.; Wada, S.; Kuroiwa, Y.; Tsurumi, T. *Appl. Phys. Lett.* **2008**, *93*, 192914.
(3) He, D.; Ding, Y.; Luo, H.; Li, C. *J. Mol. Catal.* **2004**, *208*, 267.
(4) Wilk, G. D.; Wallace, R. M.; Anthony, J. M. *J. Appl. Phys.* **2001**, *89*, 5243.
(5) Wang G.; Meng F.; Ding C.; Chu P. K.; Liu X. *Acta Biomater.*; available online at Elsevier Sciencehttp://www.elsevier.com.
(6) Shin, J. H.; Chao, C.-C.; Huang, H.; Prinz, F. B. *Chem. Mater.* **2007**, *19*, 3850.
(7) León, C.; Lucia, M. L.; Santamaría, J. *Phys. Rev. B* **1997**, *55*, 882.
(8) Garvie, R. C.; Hannink, R. H.; Pascoe, R. T. *Nature* **1975**, *258*, 703.
(9) Garvie, R. C. *J. Phys. Chem.* **1978**, *82*, 218.
(10) Zhang, J.; Ohara, S.; Umetsu, M.; Naka, T.; Hatakeyama, Y.; Adschiri, T. *Adv. Mater.* **2007**, *19*, 203.
(11) Joo, J.; Yu, T.; Kim, Y. W.; Park, H. M.; Wu, F.; Zhang, J. Z.; Hyeon, T. *J. Am. Chem. Soc.* **2003**, *125*, 6553.
(12) Zhao, N.; Pan, D.; Nie, W.; Ji, X. *J. Am. Chem. Soc.* **2006**, *128*, 10118.
(13) Bootz, A.; Vogel, V.; Schubert, D.; Kreuter, J. *Eur. J. Pharm. Biopharm.* **2004**, *57*, 369.
(14) Michel, D.; Perez, M.; Jorba, Y.; Collongues, R. *J. Raman Spectrosc.* **1976**, *5*, 163.
(15) Kwok, C.- K.; Aita, C. R. *J. Appl. Phys.* **1989**, *66*, 2756.
(16) Yashima, M.; Tsunekawa, S. *Acta Crystallogr.* **2006**, *B62*, 161.
(17) Kaneko, K.; Inoke, K.; Freitag, B.; Hungria, A. B.; Midgley, P. A.; Hansen, T. W.; Zhang, J.; Ohara, S.; Adschiri, T. *Nano Lett.* **2007**, *7*, 421.
(18) Conesa, J. C. *Surf. Sci.* **1995**, *339*, 337.

JA910712R

Journal of Power Sources 195 (2010) 4114–4118

Contents lists available at ScienceDirect

Journal of Power Sources

journal homepage: www.elsevier.com/locate/jpowsour

Short communication

Performance and durability of nanostructured $(La_{0.85}Sr_{0.15})_{0.98}MnO_3$/yttria-stabilized zirconia cathodes for intermediate-temperature solid oxide fuel cells

Kazuyoshi Sato [a,*], Toru Kinoshita [b], Hiroya Abe [a]

[a] Joining and Welding Research Institute, Osaka University, 11-1 Mihogaoka, Ibaraki, Osaka 567-0047, Japan
[b] New Technology Research Laboratory, Sumitomo Osaka Cement Co., Ltd., 585 Toyotomi-Cho, Funabashi, Chiba 247-8601, Japan

ARTICLE INFO

Article history:
Received 11 November 2009
Received in revised form
22 December 2009
Accepted 21 January 2010
Available online 25 January 2010

Keywords:
Solid oxide fuel cells
LSM/YSZ cathode
Nanostructure
Power density
Durability

ABSTRACT

In this communication we report the fabrication of nanostructured $(La_{0.85}Sr_{0.15})_{0.98}MnO_3$ (LSM)/yttria-stabilized zirconia (YSZ) composite cathodes consisting of homogeneously distributed and connected LSM and YSZ grains approximately 100 nm large. We also investigate for the first time the role of the cathode nanostructure on the performance and the durability of intermediate-temperature solid oxide fuel cells. The cathodes were fabricated using homogenous LSM/YSZ nanocomposite particles synthesized by co-precipitation, using YSZ nanoparticles of 3 nm as seed crystals. Detailed microstructural characterization by transmission electron microscopy with energy-dispersive X-ray spectroscopy revealed that many of the LSM/YSZ junctions in the cathode faced the homogeneously connected pore channels, indicating the formation of a considerable number of triple phase boundaries. The nanostructure served to reduce cathodic polarization. As a result, these anode-supported solid oxide fuel cells showed high power densities of 0.18, 0.40, 0.70 and 0.86 W cm^{-2} at 650, 700, 750 and 800 C, respectively, under the cell voltage of 0.7 V. Furthermore, no significant performance degradation of the cathode was observed during operation at 700 °C for 1000 h under a constant current density of 0.2 A cm^{-2}.

1. Introduction

Strontium-doped lanthanum manganite $(La_xSr_{1-x})_yMnO_3$ (LSM)/yttria-stabilized zirconia (YSZ) composite is a promising cathode material for solid oxide fuel cells (SOFCs) operated at 900 °C or higher. Recent research and development on SOFCs have been directed to reduce the operation temperature into the so-called intermediate range (650–800 °C), with the aim of cost reduction and durability enhancement of the cells and the system. In this temperature range, however, the oxygen reduction reaction (ORR) property of the cathode often limits the overall performance of the state-of-the-art SOFCs with a Ni/YSZ cermet anode, thin YSZ electrolyte and LSM/YSZ composite cathode [1]. Previous studies on the relationship between microstructure and performance of the composite cathode have shown that ORR occurs in the vicinity of triple phase boundaries (TPBs), where LSM, YSZ and pore phases meet [2–4]. These pioneering studies have stimulated considerable efforts in optimizing cathode microstructure for improved performance [5–8]. Recently, Wang et al. reported that the performance of intermediate-temperature SOFC (IT-SOFC) can be significantly improved by reducing the grains of the composite cathode from conventional micron size down to 100 nm [9].

Long-term stability is another important requirement of fuel cell technology. It has been reported recently that performance degradation of the LSM/YSZ cathode often dominates that of the IT-SOFCs and becomes significant rather at lower temperatures [10–12]. Liu et al. have reported that the degradation can be attributed to the formation of zirconates ($La_2Zr_2O_7$ and $SrZrO_3$) related to the chemical instability of LSM under a current load [11]. Their thermodynamic calculations suggested that the high performance LSM/YSZ cathode could suppress the formation of zirconates, thereby improving long-term stability of the cells. Furthermore, Song et al. have demonstrated that a cathode with uniformly distributed LSM and YSZ shows better long-term stability than that with a nonuniform microstructure [8].

Based on previous reports [8–12], we can predict that homogeneous nanostructured cathodes with fine LSM and YSZ grains of smaller than 100 nm are promising candidates for IT-SOFC cathodes. The nanostructure of the cathodes should be optimized not only to enhance performance, but also to maximize long-term stability. Therefore, the role of nanostructure in performance and durability must be well understood; however, it has thus far remained unclear, possibly due to the difficulty of fabrication of the nanostructured cathodes. Actually, no nanostructured cathodes

* Corresponding author. Tel.: +81 668 79 4370; fax: +81 668 79 4370.
E-mail address: k-sato@jwri.osaka-u.ac.jp (K. Sato).

0378-7753/$ – see front matter © 2010 Elsevier B.V. All rights reserved.
doi:10.1016/j.jpowsour.2010.01.045

have been reported in the literature after a report by Wang et al. [9]. For fabrication of a homogeneous nanostructured cathode using conventional particle processing, it is necessary to synthesize the starting particles, which consist of homogeneously distributed LSM and YSZ particles much smaller than 100 nm, taking into account grain growth during sintering. Virtually all LSM/YSZ composite cathodes to date can be described as a physical mixture of separately synthesized LSM and YSZ particles. However, the possible particle size for uniform mixing is above sub-micron [5], hence the grain size of the resultant cathodes is typically on the order of one to several microns. Although there are few reports on the synthesis of LSM/YSZ nanocomposite particles by build-up methods [6–8], significant grain growth during the post-sintering process resulted in sub-micron grain size. This may be due to the lack of homogeneity in the size and distribution of LSM and YSZ phases.

We have recently successfully synthesized homogeneous $(La_{0.85}Sr_{0.15})_{0.98}MnO_3$/YSZ nanocomposite particles through a novel co-precipitation method using 3-nm diameter YSZ nanoparticles as seed crystals. The cathode fabricated by nanocomposite particles consisted of grains approximately 100 nm in size. In the present study, we analyze the detailed nanostructure of these cathodes and investigate the role of nanostructure on the performance and durability of IT-SOFCs.

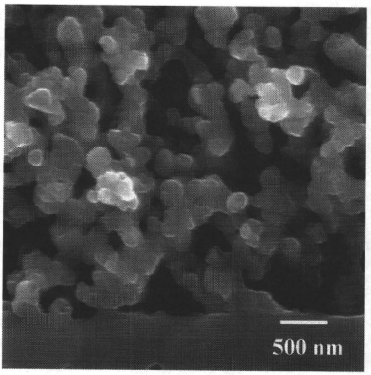

Fig. 1. A cross-sectional SEM image of the cathode/electrolyte interface of the anode-supported cell.

2. Experimental

Anode-supported and symmetric cells were fabricated using $(La_{0.85}Sr_{0.15})_{0.98}MnO_3$/YSZ nanocomposite particles. The mass fraction of LSM and YSZ in the nanocomposite was even. The detailed synthesis procedure of the composite particles was described in the previous report [13]. The anode-supported cell was fabricated in manner similar to previous studies [14,15]. Thin YSZ electrolyte (approximately 10 μm thick)/thick NiO/YSZ anode (approximately 500 μm thick) bi-layer was fabricated by tape casting, followed by co-sintering at 1350 °C for 2 h. A cathode layer 6 mm in diameter was deposited onto the thin film YSZ electrolyte by screen printing, followed by sintering at 1100 °C for 2 h. Symmetric cells were fabricated in the following manner. First, a dense YSZ electrolyte disk 13 mm in diameter and 450 μm in thickness was fabricated by tape casting, followed by sintering at 1350 °C for 2 h. Second, an LSM/YSZ layer 6 mm in diameter was deposited symmetrically on both sides of the YSZ disk using the conditions above. Platinum paste 2 mm in diameter was applied onto the counter-electrode side of the YSZ disk and sintered at 900 °C to create a reference electrode. The reference electrode was placed 3 mm away from the counter electrode.

The current density–voltage characteristics of the anode-supported cell were measured in the temperature range 650–800 °C. Air and 3% humidified hydrogen were supplied as oxidant and fuel, respectively, with flow rates of 30 l/h. The durability of the cathodes was tested using the symmetric cell at 700 °C under air flow of 30 l/h. The tests were conducted for up to 1000 h with a constant current density of 0.2 A cm^{-2} using a three electrodes-four leads geometry.

Detailed microstructure of the cathode was observed by scanning electron microscopy (SEM; ERA-8800FE, Elionix, Japan) and transmission electron microscopy (TEM; JEM-2100F, JEOL, Japan) with energy-dispersive X-ray spectroscopy (EDS; JED-2300T, JEOL, Japan).

3. Results and discussion

Fig. 1 shows the cross-sectional image of the cathode/electrolyte interface of an anode-supported cell. A well-bounded cathode/electrolyte interface can be seen. Successful low-temperature sintering may be attributed to the high surface area of the nano-sized starting particles [13]. The cathode layer consisted of fine, homogeneously connected solid stems and pore channels. Grains approximately 100 nm large were observed.

Fig. 2 shows an STEM image and corresponding EDS mappings of a thin section of the composite cathode. Well-sintered solid stems without significant grain growth may be due to the uniform size and distribution of LSM and YSZ in the starting particles. The average diameter of the solid stems determined from the length of 100 intercepts of randomly drawn lines on the several images was 445 μm, which may represent the size of secondary agglomerates of the composite particles suspended in the screen printing paste [16]. The average diameter of pore channels determined in the same manner was 220 μm. This diameter may be sufficient to diffuse gaseous oxygen, since it was greater than the mean free path of the molecules [17]. The diameter was larger than the grain size. This agrees with the previous studies on sintering, in which pores larger than the grains persist during the densification [18,19]. Porosity estimated from pore area on several TEM images was approximately 25%, and was nearly the optimum value estimated by a computational approach [17]. The distributions of La and Zr in EDS mappings are likely to represent those of LSM and YSZ phases, respectively, since any other phases such as $La_2Zr_2O_7$ and $SrZrO_3$ were not detected in the X-ray diffraction profiles, even when the composite particles were heat treated at 1100 °C [13]. The overlay image of the EDS mappings (Fig. 2(c)) shows that both LSM and YSZ had uniform grain size of about 100 nm and that the uniformly distributed phases were homogeneously connected. Note that many of LSM/YSZ junctions faced the pore channels, suggesting the formation of a large amount of TPBs. This can clearly be attributed to uniformly distributed nano-sized LSM and YSZ grains, in addition to fine and uniformly connected solid stems and pore channels.

Fig. 3 shows the current density–voltage characteristics and the corresponding power density profiles of the anode-supported cell measured between 650 and 800 °C. The open circuit voltage (OCV) was 1.068, 1.064, 1.056 and 1.050 V at 650, 700, 750 and 800 °C, respectively. It was confirmed that the slightly lower OCVs than the theoretical ones (the difference was 0.05–0.06 V) were due to some minor leakage of anode gas through glass sealant. Thus the performance will be slightly underestimated from the real one. Nevertheless, the cells exhibited the high power density

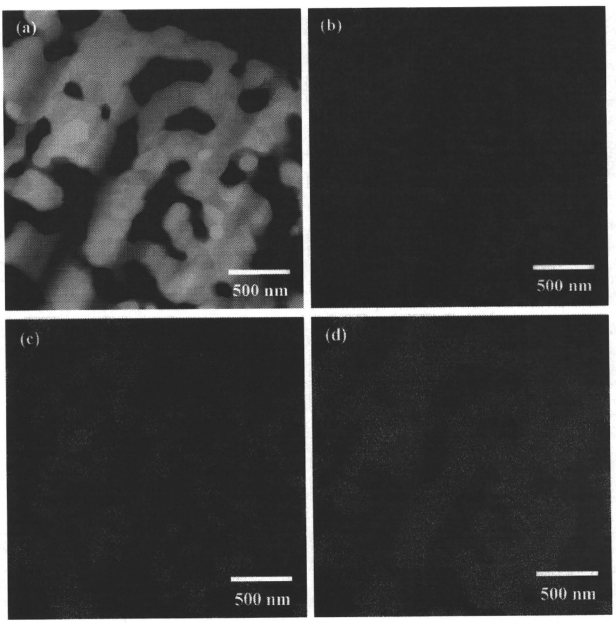

Fig. 2. (a) STEM image, (b) Zr mapping, (c) La mappings, and (d) the overlay image of Zr and La mappings of a nanostructured cathode.

of 0.20, 0.40, 0.69 and 0.85 W cm^{-2} at 650, 700, 750 and 800 °C, respectively, under the cell voltage of 0.7 V. This high performance indicates that the anode-supported cell with the present nanostructured cathode has potential to be operated at the intermediate temperature range with an acceptable power density. Clearly, the high performance can be attributed to the formation of a large amount of TPBs in the nanostructured cathode. The performance was better than that of the cells with a $La_{0.6}Sr_{0.4}Co_{0.2}Fe_{0.8}O_{3-\delta}$ (LSCF) cathode fabricated under optimized processing conditions [14,20]. Materials and processing parameters of the present thin-film YSZ electrolyte and Ni/YSZ anode, as well as the testing conditions were the same as in the previous studies. In the common sense, LSCF has superior ORR property to LSM/YSZ composite at intermediate temperature. However these facts indicated that the present nanostructured LSM/YSZ cathode has better ORR property than the LSCF cathode. The electrochemical performance of the composite cathode is no longer the bottleneck of the overall cell performance, since that of Ni/YSZ anode limited the overall performance of the cell with the LSCF cathode [14].

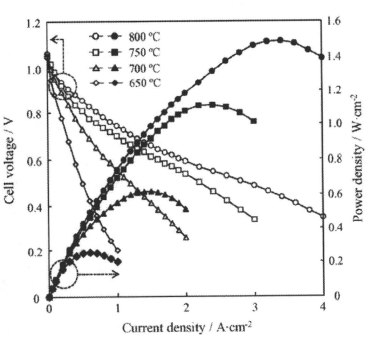

Fig. 3. Current density–voltage characteristics and corresponding power density profiles of the anode-supported cell measured between 650 and 800 °C.

Fig. 4 shows the polarization of a nanostructured LSM/YSZ cathode as a function of operation time measured using the symmetric cell at 700 °C under a current load of 0.2 A cm^{-2}. In this condition, the anode-supported cell with the nanostructured cathode can be operated at an acceptable power density of 0.2 W cm^{-2} under cell voltages above 0.8 V, as shown in Fig. 3. The cathode exhibited good long-term performance stability under the test condition. The polarization after 1000 h was almost the same as at the beginning, even though the presence of some minor perturbations which probably due to some changes in the experimental conditions such as local temperature and humidity of supplied air. Liu et al. suggest that the formation of zirconates at the cathode/electrolyte interface was responsible for the performance degradation of the cathode, and their formation can be related to the chemical instability of

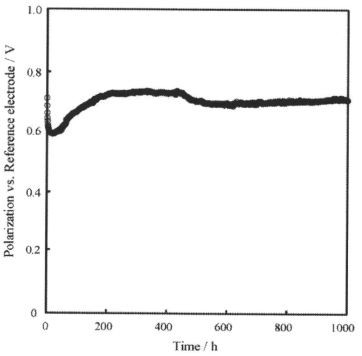

Fig. 4. Polarization of the cathode vs time under a constant current density of 0.2 A cm^{-2} at 700 °C.

LSM under a current load [11]. They estimate the risk of zirconate formation as a function of oxygen partial pressure at the interface ($p(O_{2,Interface})$) based on a thermodynamic model. The value of $p(O_{2,Interface})$ during operation can be estimated by the Nernst equation as a function of cathodic polarization and temperature [11]. Polarization of the present nanostructured LSM/YSZ cathode extracted from the total polarization of the symmetric cell using the current interruption technique [14,20] was 0.17 V at the initial stage of testing. The calculated $p(O_{2,Interface})$ was 6.30×10^{-5} atm, and is high enough to avoid the formation of zirconates at 700 °C [11].

Fig. 5 shows an SEM image of the cathode after a durability test. Although grain size stayed constant, the morphology of individual grains changed after testing. Jiang et al. reported a similar morphological change on an A-site deficient LSM cathode under a current load [21]. They reported that the morphological change causes a drastic reduction of cathodic polarization during the initial stage, as shown in Fig. 4. They suggested a possible mechanism

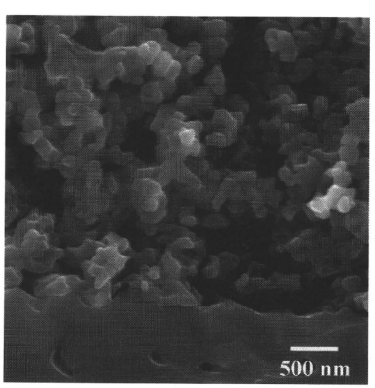

Fig. 5. A cross-sectional SEM image of the cathode/electrolyte interface after durability testing.

of the morphological change via significant generation and migration of oxygen vacancies and manganese ions on the surface and along the grain boundaries of LSM. These could weaken the contact between particles, leading to disintegration of agglomerates in the case of A-site deficient LSM. Similar phenomena may occur in the present nanostructured cathode, since the LSM in the present study is also A-site deficient. Nevertheless, despite the morphological change by surface and grain boundary diffusion, grain size remained nearly constant. This may be due to the suppression of grain boundary migration by a uniformly distributed YSZ phase within the cathode, as shown in Fig. 2. Some small cracks were observed at the cathode/electrolyte interface. Liu et al. reported that these cracks were formed due to the formation of zirconates during operation [11]. However, the analysis of a local area by SEM-EDS could not show conclusive evidence of zirconate formation. In addition, the $p(O_{2,Interface})$ was kept sufficiently high to suppress their formation, as discussed above. Further analysis is needed to clarify the detailed mechanism of formation of the local cracks. However, if we assumed that the increase in the polarization between 20 and 200 h was caused by the formation of these cracks, the constant polarization up to 1000 h suggested that they did not extend during the entire period. In summary, the present high-performance nanostructured cathodes can enhance long-term performance stability of IT-SOFCs not only by minimizing zirconate formation and crack extension at the cathode/electrolyte interface, but also by maintaining considerable amount of TPBs.

4. Conclusions

Nanostructured LSM/YSZ cathodes with fine and uniformly connected LSM, YSZ and pore phases formed a large amount of the TPBs, giving rise to high-performance IT-SOFCs. Such a high-performance nanostructured cathode can enhance the long-term performance stability by suppressing zirconate formation, crack extension and grain growth during operation. The present nanostructured LSM/YSZ is a promising cathode material for IT-SOFCs.

Acknowledgements

This work was partly supported by a Scientific Research Grant from the Ministry of Education, Science, Sports, and Culture of Japan.

References

[1] J.M. Ralph, A.C. Schoeler, M. Krumpelt, J. Mater. Sci. 36 (2001) 1161–1172.
[2] T. Kenjo, M. Nishiya, Solid State Ionics 57 (1992) 295–302.
[3] K. Sasaki, J.-P. Wurth, R. Gschwend, M. Gödickemeier, L.J. Gauckler, J. Electrochem. Soc. 143 (1996) 530–543.
[4] F.H. van Heuveln, H.J.M. Bouwmeester, F.P.F. van Berkel, J. Electrochem. Soc. 144 (1997) 126–133.
[5] J. Piao, K. Suna, N. Zhang, S. Xub, J. Power Sources 175 (2008) 288–295.
[6] J.-H. Kim, R.-H. Song, J.-H. Kim, T.-G. Lim, T.-K. Sun, D.-R. Shin, J. Solid State Electrochem. 11 (2007) 1385–1390.
[7] M. Mamak, G.S. Métraux, S. Petrov, N. Coombs, G.A. Ozin, M.A. Grees, J. Am. Chem. Soc. 125 (2003) 5161–5175.
[8] H.S. Song, S. Lee, S.H. Hyun, J. Kim, H.-W. Lee, J. Moon, J. Mater. Chem. 18 (2008) 1087–1092.
[9] W.G. Wang, Y.-L. Liu, R. Barfod, S.B. Schougaard, P. Gordes, S. Ramousse, P.V. Hendriksen, M. Mogensen, Electrochem. Solid-State Lett. 8 (2005) A619–A621.
[10] A. Hagen, R. Barfod, P.V. Handriksen, Y.-L. Liu, S. Ramousse, J. Electrochem. Soc. 153 (2006) A1165–A1171.
[11] Y.L. Liu, A. Hagen, R. Barfod, M. Chen, H.J. Wang, F.W. Poulsen, P.V. Hendriksen, Solid Sate Ionics 180 (2009) 1298–1304.
[12] A. Hagen, Y.L. Liu, R. Barford, P.V. Hendriksen, J. Electrochem. Soc. 155 (2008) B1047–B1052.
[13] K. Sato, T. Kinoshita, H. Abe, M. Naito, J. Ceram. Soc., Jpn. 117 (2009) 1186–1190.

[14] H. Abe, K. Murata, T. Fukui, W.-J. Moon, K. Kaneko, M. Naito, Thin Solid Films 496 (2006) 49–52.
[15] K. Sato, G. Okamoto, H. Abe, M. Naito, ECS Trans. 7 (2007) 1555–1561.
[16] A. Hagiwara, N. Hobara, K. Takizawa, K. Sato, H. Abe, M. Naito, Solid State Ionics 178 (2007) 1123–1134.
[17] R.E. Williford, P. Singh, J. Power Sources 128 (2004) 45–53.
[18] F.F. Lange, B.J. Kellet, J. Am. Ceram. Soc. 72 (1989) 735–741.
[19] W.D. Kingery, B. Francois, in: G.C. Kuczynski, N.A. Hooton, G.N. Gibbon (Eds.), Sintering and Related Phenomena, Gordon and Breach, New York, 1967, pp. 471–498.
[20] K. Murata, T. Fukui, H. Abe, M. Naito, K. Nogi, J. Power Sources 145 (2005) 257–261.
[21] S.P. Jiang, J.G. Love, Solid State Ionics 158 (2003) 45–53.

J Nanopart Res
DOI 10.1007/s11051-011-0324-0

RESEARCH PAPER

One-pot hydrothermal synthesis of an assembly of magnetite nanoneedles on a scaffold of cyclic-diphenylalanine nanorods

Takanari Togashi · Mitsuo Umetsu · Takashi Naka · Satoshi Ohara · Yoshiharu Hatakeyama · Tadafumi Adschiri

Received: 17 November 2010 / Accepted: 7 March 2011

Abstract The assembly of metal oxide nanoparticles (NPs) on a biomolecular template by a one-pot hydrothermal synthesis method is achieved for the first time. Magnetite (Fe_3O_4) nanoneedles (length: ~100 nm; width: ~10 nm) were assembled on cyclic-diphenylalanine (cFF) nanorods (length: 2–10 μm; width: 200 nm). The Fe_3O_4 nanoneedles and cFF nanorods were simultaneously synthesized from $FeSO_4$ and L-phenylalanine by hydrothermal synthesis (220 °C and 22 MPa), respectively. The samples were analyzed by powder X-ray diffraction (XRD), Fourier transform infrared spectroscopy (IR), transmission electron microscopy (TEM), and superconducting quantum interference device (SQUID) magnetometry. Experimental results indicate that Fe_3O_4 nanoneedles were assembled on cFF nanorods during the hydrothermal reaction. The composite contained 3.3 wt% Fe_3O_4 nanoneedles without any loss of the original magnetic properties of Fe_3O_4.

Keywords Self-assembly · Magnetite · Peptide · Hydrothermal · One-pot synthesis

Electronic supplementary material The online version of this article (doi:10.1007/s11051-011-0324-0) contains supplementary material, which is available to authorized users.

T. Togashi (✉) · T. Adschiri
Advanced Institute for Material Research,
Tohoku University, 2-1-1, Katahira, Aoba-ku,
Sendai 980-8577, Japan
e-mail: togashi@tagen.tohoku.ac.jp

M. Umetsu
Department of Biomolecular Engineering, Graduate School of Engineering, Tohoku University, Aoba 6-6-11-608 Aramaki, Aoba-ku, Sendai 980-8579, Japan

T. Naka
Innovative Materials Engineering Laboratory,
National Institute for Material Science, Sengen 1-2-1,
Tsukuba, Ibaraki 305-0047, Japan

S. Ohara
Joining and Welding Research Institute,
Osaka University, 11-1 Mihogaoka, Ibaraki,
Osaka 567-0047, Japan

Y. Hatakeyama
Institute for Multidisciplinary for Advanced Material,
Tohoku University, 2-1-1 Katahira, Aoba-ku, Sendai,
Miyagi 980-8577, Japan

Introduction

At present, it is considered that the hierarchical structures formed by the self assembly of nanoparticles (NPs) of inorganic materials such as metals, semiconductors, and ceramics can be used to develop novel electronic, magnetic, and optical devices on account of certain interactions between the excitons, magnetic moments, or surface plasmons of individual NPs (Nie et al. 2010). Many research groups have reported the assembly of isotropic 2D and 3D NPs using various techniques to form structures such as

Published online: 23 March 2011

films/sheets and superlattice crystals (Pileni 2001; Collier et al. 1998; Claridge et al. 2009; Gasser 2009). In contrast, few studies have demonstrated the assembly of anisotropic structures such as rods or fibers, probably on account of the difficulties involved in the preparation of such structures along anisotropic directions (Tang and Kotov 2005).

Biomaterials are highly ordered from the molecular scale to the nano- and microscales, often in a hierarchical manner; most functional hard tissues are characterized by intricate nanostructure comprising biomolecules and inorganic materials (Sarikaya et al. 2003). It is anticipated that biomolecules can serve as highly powerful tools in the development of scaffolds for NP assembly. In general, inorganic NPs tend to aggregate because of their high surface energy. Consequently, prior to assembly, a solution containing completely dispersed NPs must be prepared. However, the requirement for completely dispersed NPs can be bypassed by the formation of NPs on or in a biomolecular scaffold substrate.

To prepare anisotropic NP assemblies, self-assembling biomolecules such as DNA (Braun et al. 1998; Alivisatos 2004; Hatakeyama et al. 2004), peptides (Banerjee et al. 2005; Sone and Stupp 2004; Fu et al. 2003; Carny et al. 2006), proteins (Scheibel et al. 2003; Patolsky et al. 2004; Platt et al. 2005; Ostrov and Gazit 2010), and polysaccharides (Feng et al. 2005; Wang et al. 2009; Huang and Kunitake 2003) have been used; these biomolecules are utilized not only in applications involving cell manipulation (Hultgren et al. 2003) and drug delivery (Tan et al. 2006) but also as templates for the arrangement of inorganic NPs. In general, approaches involving biomolecular assembly are carried out in aqueous solutions under physiologically mild conditions, because biomolecules are typically hydrophobic and heat-labile. However, a high temperature is usually required to obtain high-quality inorganic material.

In our previous study, we synthesized cyclic-diphenylalanine (cFF) crystals from L-phenylalanine (L-Phe) with a high yield by hydrothermal treatment, and we found that excess cFF synthesis caused the spontaneous assembly of cFF crystals with a rod-like morphology (Togashi et al. 2006). Interestingly, the reaction conditions used for the synthesis of cFF nanorods can also be utilized to synthesize organic modified metal oxide NPs (Byrappa and Adschiri 2007; Yoshimura and Byrappa 2008). We consider that cFF nanorods and metal oxide NPs can be simultaneously synthesized and that cFF nanorods can be utilized as a template for metal oxide NP assembly.

In this report, we propose a one-pot synthesis method to assemble metal oxide NPs on a biomolecular template in water at high temperature and pressure. L-Phe and iron ions were used for synthesizing cFF and magnetite (Fe_3O_4) NPs, respectively. In addition, the synthesized Fe_3O_4 was conjugated on cFF rods during the reaction.

Experimental

Chemicals

L-Phenylalanine (L-Phe) and iron sulfide ($FeSO_4$) and potasium hydroxide (KOH) were purchased from Wako Pure Chemical Industries Ltd. and used without further purification.

Synthesis

A pressure-resistant tube reactor (SUS 316) with an inner volume of 5.0 mL was used for the hydrothermal synthesis of cFF and the cFF–Fe_3O_4 conjugate. For synthesizing the cFF–Fe_3O_4 conjugate, 0.49 g of L-Phe powder was placed in the reactor, after which 2.14 mL of 100 mM $FeSO_4$ aqueous solution and 2.14 mL of 200 mM KOH aqueous solution were added and the reactor was heated in an electric furnace controlled at 220 °C to carry out the reaction. The estimated pressure inside the reactor at 220 °C is 22 MPa. After 30 min, the reaction was terminated by cooling the reactor in a water bath at room temperature. The products were washed by three cycles of centrifugation at 9200*g* for 30 min, decantation, and redispersion into double distilled water (ddH_2O) to remove unreacted L-Phe and water-soluble chemicals. The obtained products were dried under vacuum at room temperature. For synthesizing cFF and Fe_3O_4 NPs, the $FeSO_4$ and KOH solution was replaced with water and the concentration of L-Phe was varied in the range 0–100 mM, respectively.

Analysis

Transmission electron microscopy (TEM) and high-resolution TEM (HRTEM) were performed on a JEM-1200 EXII electron microscope (JEOL Ltd., Japan) operating at 120 kV and a Hitachi H-7100 electron microscope (Hitachi Inc, Japan) operating at 200 kV, respectively. The samples were dispersed in ddH_2O and the dispersed samples were dropped on a carbon-coated copper grid. For the products, attenuated total reflectance Fourier transform infrared (ATR FT-IR) spectra were measured on a FT/IR680 spectrometer (Jasco Corp., Japan). Powder X-ray diffraction (XRD) patterns of the products were recorded on a Rigaku RINT 2000 system (Rigaku, Japan) using Cu Kα radiation at 2θ values ranging from 10° to 80°. The oriented particulate monolayer XRD (OPML-XRD) method was also employed to analyze the sample. To prepare the sample for OPML-XRD, a few drops of 3 wt% gelatine solution containing 1 wt% sample powder was evenly spread over a glass plate and dried overnight at room temperature; by using this procedure, the direction of alignment of the elongated crystals could be controlled such that it was parallel to the plane of the glass plate.

Result and discussion

In order to analyze the crystal growth direction of the cFF nanorods in the precipitates synthesized by the hydrothermal reaction of L-Phe without $FeSO_4$, the products were analyzed using powder X-ray diffraction (XRD) and the OPML-XRD method (Fig. 1). The powder XRD pattern of the products (Fig. 1b) was similar to the diffraction pattern of single cFF crystals calculated using the single crystal geometry data for cFF reported by Gdaniec et al. (Fig. 1a) (Gdaniec and Liberek 1986). The OPML-XRD pattern (Fig. 1c) revealed three peaks that were assigned to the diffractions of the (012), (024), and (018) facets of the cFF crystal. The OPML-XRD method was used to estimate the Miller indices of the facets of the polyhedral microcrystals, the basal plane of the pellet particle, and the evolution axis of elongated particles (Sugimoto et al. 1993). The estimation results revealed that anisotropic crystals were laid on the glass plate surface, with their axes

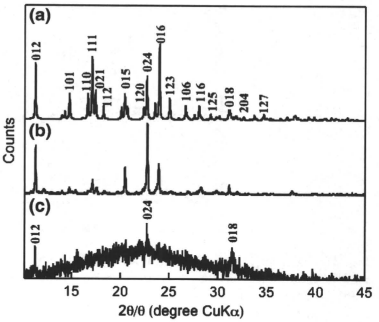

Fig. 1 XRD pattern of cFF. (*a*) Diffraction pattern calculated using single crystal geometry data, (*b*) XRD pattern of cFF synthesized by hydrothermal reaction at 220 °C and 22 MPa for 30 min, and (*c*) OPML-XRD pattern of synthesized cFF

positioned parallel to the plane of the glass plate, thereby indicating that the cFF nanorods grew along the *x*-axis. Figure 2 shows the single crystal geometry of cFF. Intermolecular hydrogen bonds of diketopiperadine are formed through amide group linkages along the *x*-axis. These intermolecular hydrogen bonds of the amide groups may serve as a driving force in the formation of anisotropic cFF nanorods (Fig. 2).

Figure 3 shows photographs of the products that were obtained by the hydrothermal treatment of L-Phe and $FeSO_4$ solutions at 220 °C and 22 MPa for 30 min. As previously reported, the hydrothermal treatment of 100 mM L-Phe solution led to the synthesis of a small amount of cFF (Togashi et al. 2006), but an increase in the L-Phe concentration to 710 mM led to the synthesis of a large amount of cFF (Fig. 3a(i)). The hydrothermal reaction of 100 mM L-Phe in a 50 mM $FeSO_4$ solution resulted in the formation of a black-colored insoluble product (Fig. 3a(ii)); however, an increase in the L-Phe concentration to 710 mM led to the formation of a brown-colored aggregate (Fig. 3a(iii)). The black- and brown-colored products synthesized in the 50 mM $FeSO_4$ solution were attracted toward a permanent magnet generating a magnetic field of 0.35 T at the magnet surface (Fig. 3b), while the aggregates synthesized without $FeSO_4$ were not attracted by the applied external magnetic field

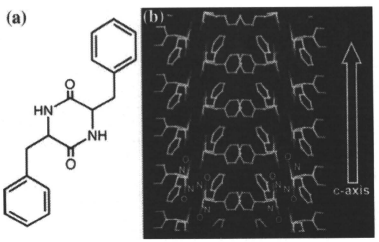

Fig. 2 (*a*) Chemical structure of L-Phe (*b*) Rod-like assembly model of the single crystal structure (This figure appear in color in online, *yellow*: carbon atom, *blue*: nitrogen atom, *red*: oxygen atom)

(Fig. 3(i)). These results imply the formation of a magnetic iron oxide such as magnetite (Fe_3O_4) or maghemite (γ-Fe_2O_3) during the hydrothermal reaction.

The powder XRD patterns of the products (Fig. 4) were measured in order to identify magnetic materials in the black- and brown-colored products synthesized from L-Phe with $FeSO_4$ (Fig. 4). The black-colored products synthesized from 100 mM L-Phe in 50 mM $FeSO_4$ could satisfactorily be assigned to spinel-type iron oxide, Fe_3O_4, or γ-Fe_2O_3 (Fig. 4a). Further, the crystalline phase was identified as Fe_3O_4 from the lattice parameter calculated using the d-value of the {311} plane; this parameter was evaluated to be 8.40 Å on the basis of the reported lattice parameters of γ-Fe_2O_3 (8.346 Å; JCPDS: 39-1346) and Fe_3O_4 (8.396 Å; JCPDS: 79-4190). Thus, the synthesized magnetic materials were identified as Fe_3O_4. The powder XRD pattern of the brown-colored products revealed small diffraction peaks that were assigned to the (220), (311), and (440) planes of spinel-type iron oxide (closed circles in Fig. 4c), whereas it also revealed some intense peaks in the lower angle region (10–30°) that were well matched with those of cFF (Fig. 4b, c).

To obtain additional data for characterization of spinel-type iron oxide, the brown-colored product was measured by FT-IR spectrum. Before measurement, the brown-colored product was washed with dimethyl sulfoxide (DMSO) and methanol to remove cFF that included in brown-colored product, and the color of the obtained sample was black (see Fig. S1 in Supporting Information). Figure 5 shows the FT-IR spectra of purchased Fe_3O_4, γ-Fe_2O_3, these are used as references, and samples that were obtained from brown-colored products by washing with DMSO. The IR-spectrum of purchased Fe_3O_4, one broad peak at 578 cm^{-1} can be seen and this band is assigned as Fe–O bond of Fe_3O_4 (Fig. 5a) (Cornell and Schwertmann 2003). In the IR spectrum of γ-Fe_2O_3, the broad bands at 698, 638, 580, and 562 cm^{-1} can be seen (Fig. 5b) these are assigned as Fe–O bond of γ-Fe_2O_3 (Cornell and Schwertmann 2003). The IR spectrum of sample has broad band at 576 cm^{-1} and no additional peaks (Fig. 5c). This result strongly support to assignment of the contained iron oxide as Fe_3O_4. Therefore, we conclude that the brown-colored products were composed of Fe_3O_4 and cFF.

To observe the morphology of the synthesized Fe_3O_4 particle and cFF–Fe_3O_4 conjugate, transmission electron microscopy (TEM) images were obtained (Figs. 6, 7). Figure 6a shows the TEM

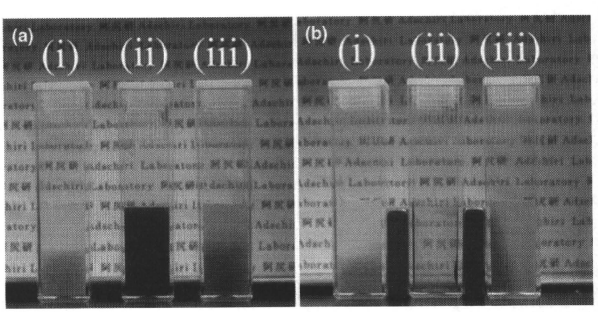

Fig. 3 Photographs of the synthesized products in a plastic cuvette. The products were synthesized by hydrothermal treatment of (*i*) 710 mM L-Phe, (*ii*) 100 mM L-Phe and 50 mM $FeSO_4$, and (*iii*) 710 mM L-Phe and 50 mM of $FeSO_4$ at 220 °C and 22 MPa for 30 min. *Left*: Without external magnetic field. *Right*: With external magnetic field for 5 min

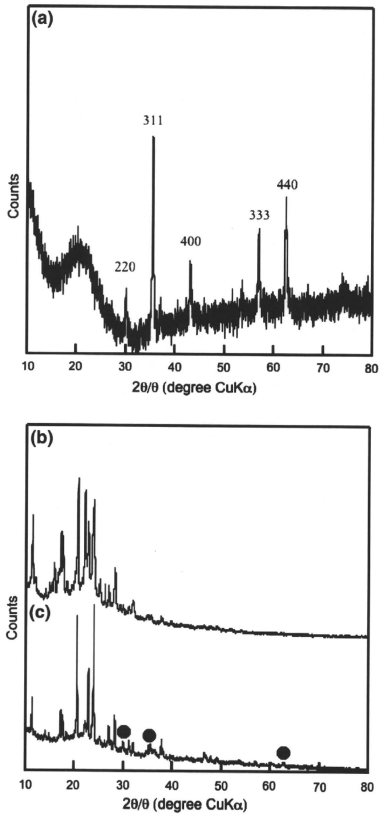

Fig. 4 XRD patterns of the crystals synthesized using (*a*) 100 mM L-Phe and 50 mM $FeSO_4$, (*b*) 710 mM L-Phe, and (*c*) 710 mM L-Phe and 50 mM $FeSO_4$

image of Fe_3O_4 synthesized from 100 mM L-Phe in 50 mM $FeSO_4$. The image reveals needle-like structures with widths and lengths of ~10 and ~100 nm, respectively. The distance between two adjacent points perpendicular to the long axis of a Fe_3O_4 nanoneedle is ~3 Å (Fig. 6b), which corresponds to the lattice spacing of the (220) plane of Fe_3O_4.

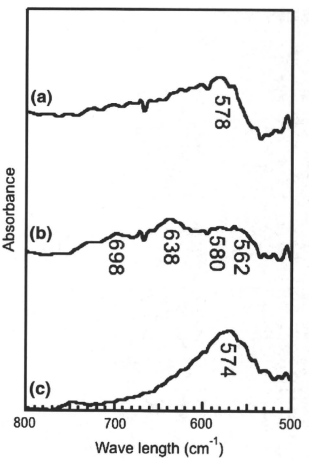

Fig. 5 FT-IR spectrum of (*a*) purchased Fe_3O_4, (*b*) purchased γ-Fe_2O_3, and (*c*) sample

Fe_3O_4 particles synthesized by hydrothermal treatment without L-Phe have spherical or cubic shapes with particle sizes ranging from 50 nm to 100 nm (see Fig. S2a in Supporting Information). As the concentration of L-Phe is increased, the particle shape changes from a spherical shape to a needle-like shape (see Fig. S2b and c in Supporting Information). The order of surface energy of the different facets is $\{111\} < \{100\} < \{110\}$ for the fcc structure (Fan et al. 2009); therefore, the organic molecules predominantly bind to the facet that has a higher surface energy (Xia et al. 2009). Our results suggest that the capping of L-Phe on the (110) surface suppressed the growth of the (220) plane.

Figure 7 shows the TEM images of the synthesized cFF–Fe_3O_4 conjugate. The materials have large rod-like morphologies with widths of 200 nm and lengths of 2–10 μm (Fig. 7a), into which needle-shaped Fe_3O_4 particles are stacked (Fig. 7b). Previously, we reported that the hydrothermal treatment of 710 mM L-Phe in ddH_2O resulted in the formation of a cFF aggregate with a rod-like morphology such that the particles had diameters of 200–500 nm and lengths of 5–10 μm (Togashi et al. 2006). The